Effect of initial preform porosity on solid-state foaming of titanium

N.G.D. Murray[a)] and D.C. Dunand[b)]

Department of Materials Science and Engineering, Northwestern University, Evanston, Illinois 60208

Titanium foams were produced by the expansion of pressurized argon pores trapped within a preform during a previous powder-consolidation step. Compared with creep expansion at 903 °C, superplastic expansion (induced by a 830–980 °C cycling around the allotropic temperature of titanium) increases foaming rate and final porosity. The pore size and fraction in the preforms were varied by using a range of initial titanium powder sizes and argon pressures. As initial preform porosity increases from 0.06 to 2.7%, foaming rate increases in the early stages of creep and superplastic foaming. However, at a later stage, foaming ceases prematurely for preforms with high initial porosity, as pores connect to the surface, allowing the escape of the pressurized argon. Preforms with 0.40% initial porosity result in foams with an optimal combination of high foaming rate, high final porosity (up to 47%), tailorable open or closed porosity, and Young's modulus as low as 23 GPa.

I. INTRODUCTION

To date, titanium and its alloys have not been foamed in the liquid state because of their high melting temperature and their extreme chemical reactivity at elevated temperatures, leading to contamination and embrittlement. Rather, as reviewed in Ref. 1, porous titanium has been produced by solid-state processes based on sintering of titanium powders or on expansion of entrapped pores. The latter method, which has been used for commercial-purity titanium (CP-Ti) and the alloy Ti-6Al-4V,[2–12] consists of two steps. First, powders are densified by hot isostatic pressing (HIPing) in the presence of argon gas within a sealed canister. The resulting compacted preform, in which a small-volume fraction (typically <3 vol%) of discreet, micron-sized pores filled with high-pressure argon is entrapped, is then foamed by heating at ambient pressure or in vacuum, allowing for the expansion of the pressurized pores by creep of the surrounding metal. Compared with foaming by pore expansion in the liquid state used for low-melting metals,[13] foaming by pore expansion in the solid is much slower and leads to lower porosity (up to 30%[10]), as creep deformation controls resistance to flow of the matrix surrounding the pores. In previous publications,[7–11] we demonstrated that

a decrease in flow resistance, and thus an increase in foaming rate and maximum achievable porosity, could be achieved by inducing superplasticity in the titanium matrix during foaming. We used transformation superplasticity,[14] where deformation occurs when internal stresses, created during a phase transformation by the density mismatch between the two coexisting allotropic phases, are biased by an externally applied stress. In the case of foaming, this biasing stress is provided by the argon pressure within the pores of the preforms. We showed that foaming CP-Ti while thermally cycling about the allotropic temperature where transformation superplasticity is activated leads to faster foaming rates and higher terminal porosities (up to 50%[7,12]) than under creep-dominated, isothermal conditions.

In previous work on CP-Ti foaming, we compared superplastic and creep expansion in terms of pore fraction, connectivity, and morphology,[8] and we studied the effect of the two main superplastic process variables (thermal cycling temperatures and rates) on pore growth kinetics and total achievable porosity.[10,11] In the present article, we investigate the effect of the two main materials variables (argon backfill pressure and titanium powder size) upon pore growth kinetics and total achievable porosity during the solid-state foaming of CP-Ti by thermal cycling and isothermal anneal.

II. EXPERIMENTAL PROCEDURES

To achieve a range of initial pore sizes, spacing, and volume fractions in the preforms, one type of unsieved

---

[a)]Formerly N.G. Davis. Present address: Stryker Howmedica Osteonics, Mahwah, NJ 07430.
[b)]Address all correspondence to this author.
 e-mail: dunand@northwestern.edu

spherical CP-Ti powder and five types of sieved spherical CP-Ti powders were used, as summarized in Table I. These powders were packed and sealed in evacuated steel canisters back-filled with high purity argon with 3.3 atm pressure at ambient temperature. A higher argon pressure of 7 atm was also used for the coarsest (400 μm) and the finest (30 μm) powders types. The sealed powders were densified by HIPing at 890 °C under 100 MPa pressure for 120 min.

Cubic specimens with 9-mm edges were cut from the densified preforms by electrodischarge machining. Their density was determined by Archimedes measurements in water, and their initial porosity was calculated from the density of CP-Ti (4.51 g/cm^3), while neglecting the density of argon (which introduces a relative error of about 8%). Foaming was performed in a Mo-element vacuum furnace or in a custom-built[15] radiative furnace under a flowing argon atmosphere with a 300 °C burn-off for 1 h and a ramp-rate from 300 to 830 °C of 75 °C/min. For 30-μm powder specimens, foaming was performed under flowing high-purity argon in a push-rod dilatometer with a temperature ramp-rate of 15 °C/min. These specimens were coated with a thin layer (about 0.1 mm) of Delta-glaze 153^{TM}, a borosilicate glass from Acheson Colloids (Port Huron, MI) used to protect titanium from contamination by residual oxygen and nitrogen, which was assumed to not affect the kinetics of titanium foaming, or to entrap gas liberated from pores connecting to the surface. Dilation of one dimension of the specimen was recorded in situ for the duration of the experiment, from which specimen volume and porosity were calculated assuming isotropic expansion.

For superplastic foaming experiments, specimens were thermally cycled between 830 and 980 °C, spanning the allotropic temperature range of CP-Ti (nominally at 882 °C, but expected to be higher and wider from oxygen content). Most thermal cycles had a 4-min period, whereas a few had a longer period of 20 min. Isothermal foaming experiments were performed at 903 and 980 °C, the effective and maximal temperatures of the

830 to 980 °C thermal cycles, respectively. The effective temperature is defined as the temperature at which the isothermal creep rate is the same as the time-averaged creep rate during thermal cycling in the absence of transformation superplasticity,[16] and it was calculated by using lattice activation energies given in Ref. 17 for α-Ti and β-Ti. Thus, by comparing the thermal cycling foaming kinetics with those performed isothermally at the effective temperature, the effect of superplasticity on foaming is directly revealed.

Except for the dilatometric experiments, foaming experiments were periodically interrupted to determine specimen density by the Archimedes method in distilled water. A thin layer of vacuum grease was applied to seal the surface of each specimen and to prevent water infiltration into the open porosity. Density measurements were also performed using helium pycnometry on unsealed specimens, allowing for measurement of closed porosity. Open porosity was calculated as the difference between total porosity (Archimedes method) and closed porosity (helium pycnometry).

After foaming completion, specimens were cut in half along one of the cube face diagonals using a low-speed diamond saw, mounted in acrylic resin, and polished to 0.05 μm alumina. Metallographic specimens were vacuum-infiltrated with the same acrylic resin used to mount the specimens at regular intervals during polishing to fill open porosity so as to retain the original pore shape during polishing.

III. RESULTS

Specimen characteristics are given in Table II in terms of process parameters (titanium powder size and backfill argon pressure in canister), preform structure before foaming (initial porosity and pore size), and foam structure after foaming (total porosity, relative open porosity ratio, and average pore size).

Based on initial powder size d, densified preforms can be assigned to four groups (Table II): coarse powders ($d = 400$ μm), intermediate-size powders ($d = 165$, 115, and 75 μm), unsieved powders ($d < 177$ μm), and fine powders ($d = 30$ μm). Within the intermediate-size powder group, the initial pore structures are similar, and, as shown below, the foaming behaviors are too. Therefore, in the following, as in Fig. 1, only one representative specimen from the intermediate-size powders group is described.

Alternatively, based on their initial porosity f_o, preforms can be separated into four groups (Table II): high initial porosity ($f_o = 2.1$–2.7%), made with the finest ($d = 30$ μm) and coarsest ($d = 400$ μm) sieved powders with the higher canister backfill argon pressure (7 atm); intermediate initial porosity ($f_o = 1.3$–1.5%), made with the same powders as above, but with the lower backfill

TABLE I. Titanium powder size characteristics.

| Powder average size[a] (μm)	Powder mesh	Powder size range (μm)	Powder median size (μm)	Powder supplier
30	−400/+500	25–37	31	TS&T[b]
75	−200/+230	62–88	75	Starmet[c]
115	−120/+140	105–125	115	Starmet
165	−80/+100	149–177	163	Starmet
400	−35/+40	355–500	423	TS&T[b]
<177	−80	<177	130	Starmet[c]

[a]Rounded median values, used in text to describe powders.
[b]TS&T, Ti Science & Technology (Xian, China). Composition from supplier (wt%): Fe, 0.06; O, <0.10; C, 0.02; N, 0.02; H, < 0.01; Ti, balance.
[c]Starmet (Concord, MA). Composition from supplier (wt%): Fe, 0.14; O, 0.14; C, 0.01; N, 0.01; H, <0.01; Ti, balance.

TABLE II. Process parameters (powder size and canister backfill pressure), preform structure before foaming (initial porosity and pore size), and foam structure after foaming (total porosity, relative open porosity ratio, and average pore size) under isothermal or thermal cycling conditions.

Initial process parameters		Preform structure		Foaming conditions	Foam characteristics			
Powder average size d (μm)	Canister backfill pressure p (atm)	Initial porosity f_o (%)	Initial pore size D_o (μm)	Foaming temperature (°C)	Maximal porosity f_{max} (%)	Time to reach f_{max} (h)	Relative open porosity ratio[a] R (−)	Final pore size[a] D (μm)
30	3.3	1.3	6 ± 3	903[b]	24	1	0.91	…
				830–980[c]	30	1.5	0.76	50
	7	2.1	7 ± 6	903[b]	24	0.3	0.73	20
				830–980[c]	35	0.3	0.74	50
75	3.3	0.14	6 ± 5	903	9[d]	25	0.10	50
				830–980	44	30	0.88	300
115	3.3	0.10	13 ± 8	903	8[d]	25	0.09	50
				830–980	44	30	0.70	200
165	3.3	0.06	12 ± 8	903	7[d]	25	0.15	50
				830–980	44	50	0.95	350
<177	3.3	0.40	12 ± 7	903	19[d]	20	0.03	200
				830–980	47	8	0.93	300
400	3.3	1.5	73 ± 30	903	10	1	0.76	…
				830–980	14	6	0.66	500
	7	2.7	50 ± 30	903	5	1	0.84	…
				830–980	13	27	0.76	300

[a]Measured at maximum porosity f_{max}.
[b]15 °C/min heating rate; all others 75 °C/min.
[c]20-min cycles; all other 4-min cycles.
[d]Porosity after given time, not terminal porosity.
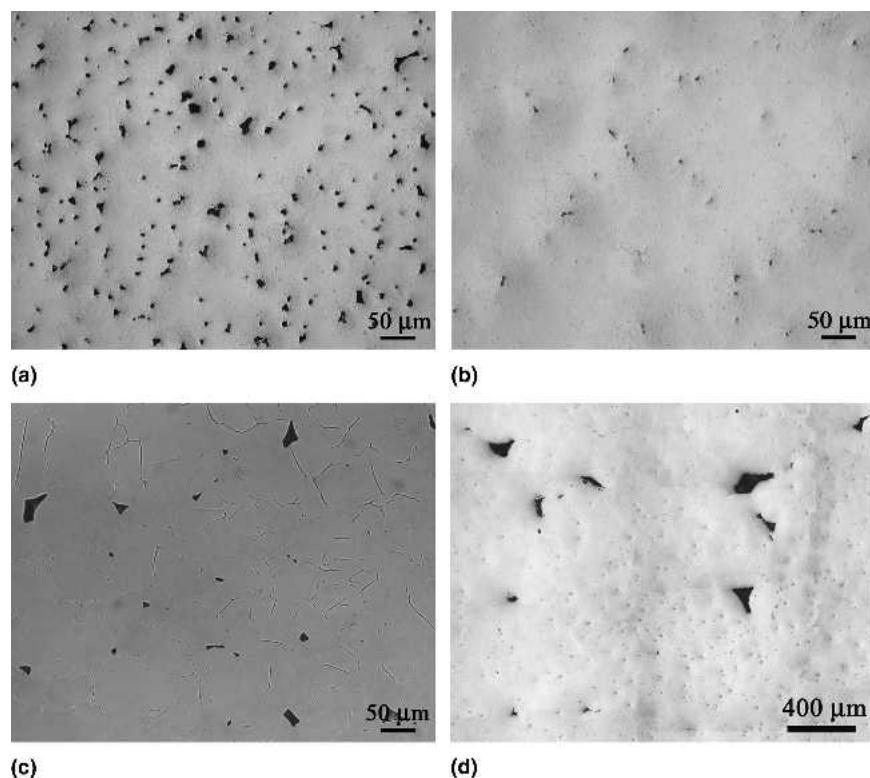
FIG. 1. Optical micrographs showing argon-pressurized pores before foaming with the following characteristics: (a) fine powders, high porosity (d = 30 μm, f_o = 2.1%); (b) intermediate powders, very low porosity (d = 75 μm, f_o = 0.14%); (c) unsieved powders, low porosity (d < 177 μm, f_o = 0.40%); and (d) coarse powders, intermediate porosity (d = 400 μm, f_o = 1.5%).

pressure (3.3 atm); low porosity ($f_o = 0.40\%$), made with unsieved powders ($d < 177$ μm); and very low initial porosity ($f_o = 0.06$–0.14%), made with intermediate-size sieved powders ($d = 75$, 115, and 165 μm). Figures 1(a)–1(d) show the initial pore structure for each of the preform groups. Finally, based on initial pore size (Table II), two groups of preforms exist: large pore size ($D_o = 50$–73 μm), made with the coarsest powders ($d = 400$ μm), and small pore size ($D_o = 6$–12 μm), made with all other powders.

A. Kinetics of porosity evolution

1. Total porosity

Figure 2 shows the isothermal foaming characteristics for all preforms, where the continuous, solid curves for the fine ($d = 30$ μm) powders specimens are from dilatometry, whereas the data points for the other specimens are Archimedes porosity measurements (dotted lines connect points to aid the eye rather than express continuous data, as for the two dilatometric lines). The fine-powder specimens remained nearly cubic in shape after foaming (minimal anisotropic expansion or face bulging), allowing use of uniaxial dilatometry data for density determination. For the other specimens, porosity as calculated from dilatometry data was only in agreement with Archimedes measurements for porosities below approximately 20%, after which specimen face bulging caused dilatometry data to overpredict porosity.

It is apparent from Fig. 2 that the initial foaming rate is very high and increases with initial preform porosity. The final porosity (listed in Table II) also increases with initial porosity, with the exception of the coarsest ($d = 400$ μm) powder preforms, which exhibit anomalously low final porosity. Indeed, the finest and coarsest powder preforms with similar initial porosity (2.7 and 2.1%, respectively) show widely different final porosities (24 versus 5%, respectively).

Figure 3 shows, for all preforms, total porosity as a function of time for the first 70 h of thermal-cycling experiments. As for isothermal experiments, the initial foaming rate is very high, it increases with increasing initial porosity, and the finest and coarsest powder preforms (with similar high initial porosity) exhibit vastly different final porosities: about 35 and 13%, respectively. The foams with the lowest initial porosity ($f_o = 0.06$–0.14%) have the slowest foaming rates of all initial conditions, but their terminal porosities reaches 44%, much higher than that of the finest or coarsest powder preforms with higher initial porosity. The unsieved-powders preform (with low initial porosity $f_o = 0.40\%$) has an intermediate foaming rate, but yields the highest final porosity, about 47%, after 12 h of thermal cycling.
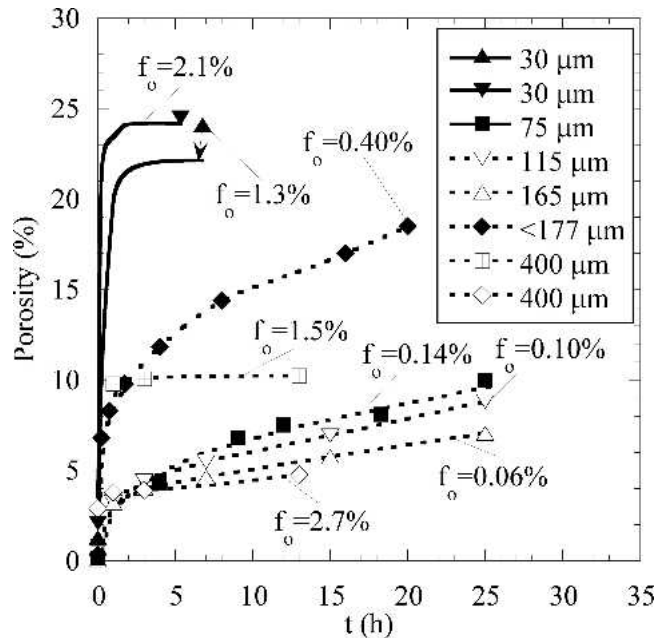

FIG. 2. Total porosity as a function of time for isothermal foaming (903 °C) for all specimens. Solid curves for 30-μm powder preforms correspond to continuous dilatometry measurements with initial heating rates of 15 °C/min, whereas all other data correspond to heating rates of 75 °C/min. Data points are from porosity Archimedes measurements and are connected with a dotted line to guide the eye.

Foaming curves for thermal cycling and isothermal conditions are compared in Figs. 4(a)–4(d) for preforms from all four groups of powder sizes, corresponding to three groups of initial preform porosity (very low, low, and intermediate f_o). The solid and dashed curves in
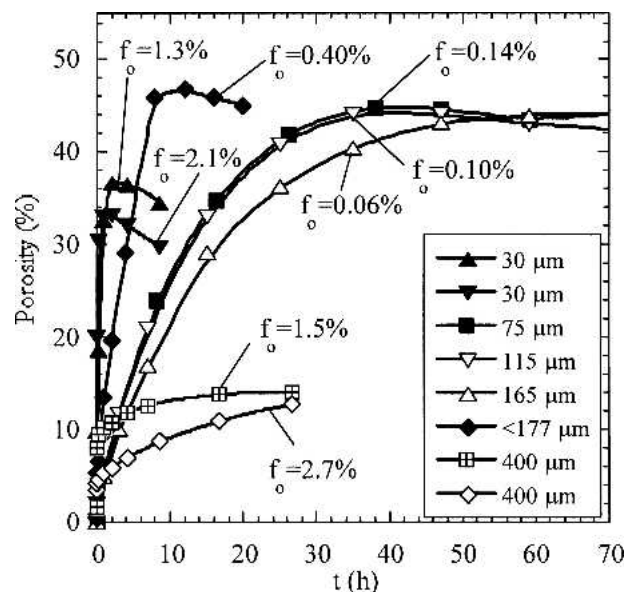

FIG. 3. Total porosity as a function of time for thermal cycling foaming (830–980 °C) for all specimens. Lines connect data points measured by the Archimedes period.
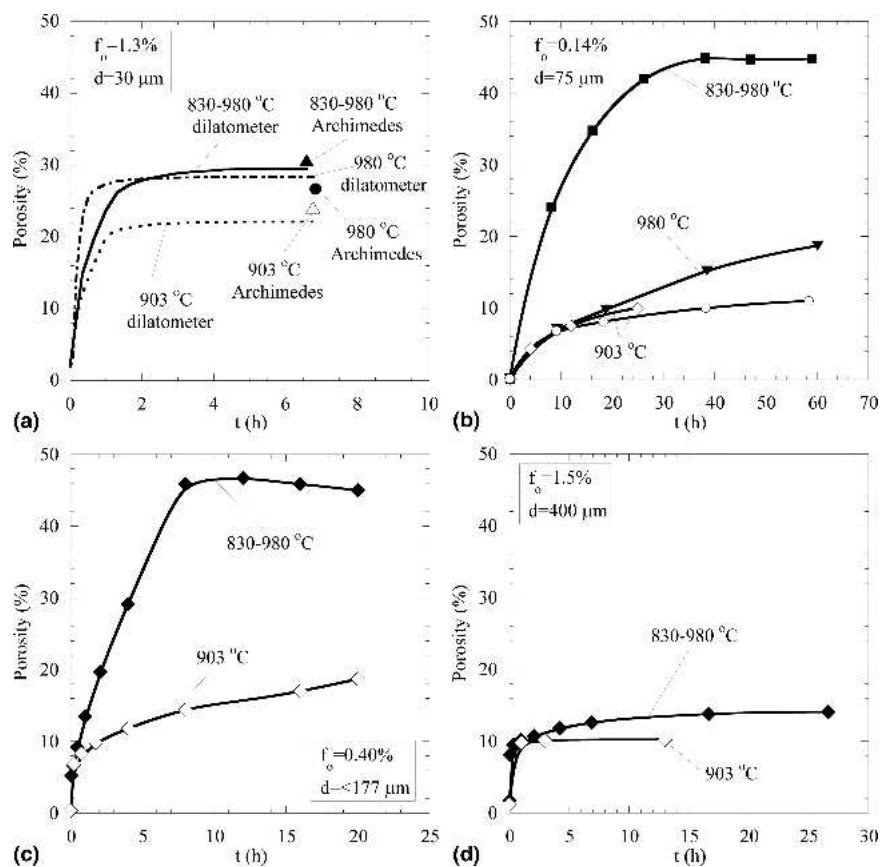
FIG. 4. Total porosity as a function of time comparing thermal cycling (830–980 °C) and isothermal foaming (903 and 980 °C) for performs with the following characteristics: (a) fine powders, intermediate porosity ($d = 30$ μm, $f_o = 1.3\%$); (b) intermediate powders, very low porosity ($d = 75$ μm, $f_o = 0.14\%$); (c) unsieved powders, low porosity ($d < 177$ μm, $f_o = 0.40\%$); and (d) coarse powders, intermediate porosity ($d = 400$ μm, $f_o = 1.5\%$).

Fig. 4(a) are from dilatometry experiments, where the heating and cooling rate for isothermal and thermal cycling was 15 °C/min. The individual data points in Fig. 4(a) are porosity measured at room temperature by the Archimedes method after foaming completion. All other data shown in Figs. 4(b)–4(d) are from Archimedes porosity measurements taken during room temperature excursions with 75 °C/min heating and cooling rates. Figures 4(a)–4(d) show that the foaming rates and terminal porosities were always higher for thermal cycling than for isothermal foaming; because the effective temperature of 903 °C was used for the latter tests, this demonstrates directly the improvement achieved by superplastic foaming. Even when comparing with the maximum temperature of the thermal cycle (980 °C), superplastic foaming under thermal cycling conditions is more rapid, with the only exception of the initial foaming rate at 980 °C in Fig. 4(a) for preforms with intermediate initial porosity ($f_o = 1.3\%$). Additionally, preforms with high initial porosity ($f_o = 2.1\%$, not shown in Fig. 4) derive almost no enhancement from thermal cycling in total porosity or foaming rate over either isothermal temperature.

2. Open and closed porosity

Open, closed, and total porosity are shown in Figs. 5(a)–5(d) as a function of foaming time under thermal cycling conditions for preforms from all four groups groups of powder sizes, corresponding to three groups of initial preform porosity (very low, low, and high f_o). All preforms exhibit fully closed porosity after HIPing, except for the coarse ($d = 400$ μm) powder preform, one-third of whose initial porosity is open. For very low and low porosity preforms [$f_o = 0.14$ and 0.40%, Figs. 5(b) and 5(c)], porosity remains closed up to relatively high values of total porosity, indicating that pores expand without connecting to the specimen surface. Thereafter, open porosity increases with foaming time, as expected if pressurized pore coalesce to the surface where the entrapped argon can escape. For high porosity preforms [$f_o = 2.1$ and 2.7%, Figs. 5(a) and 5(d)], open porosity increases immediately upon the onset of foaming, but later decreases, indicative of a densification process.

To compare the evolution of open porosity between various foams, the relative open porosity ratio F (defined as the ratio of open to total porosity) is plotted as a
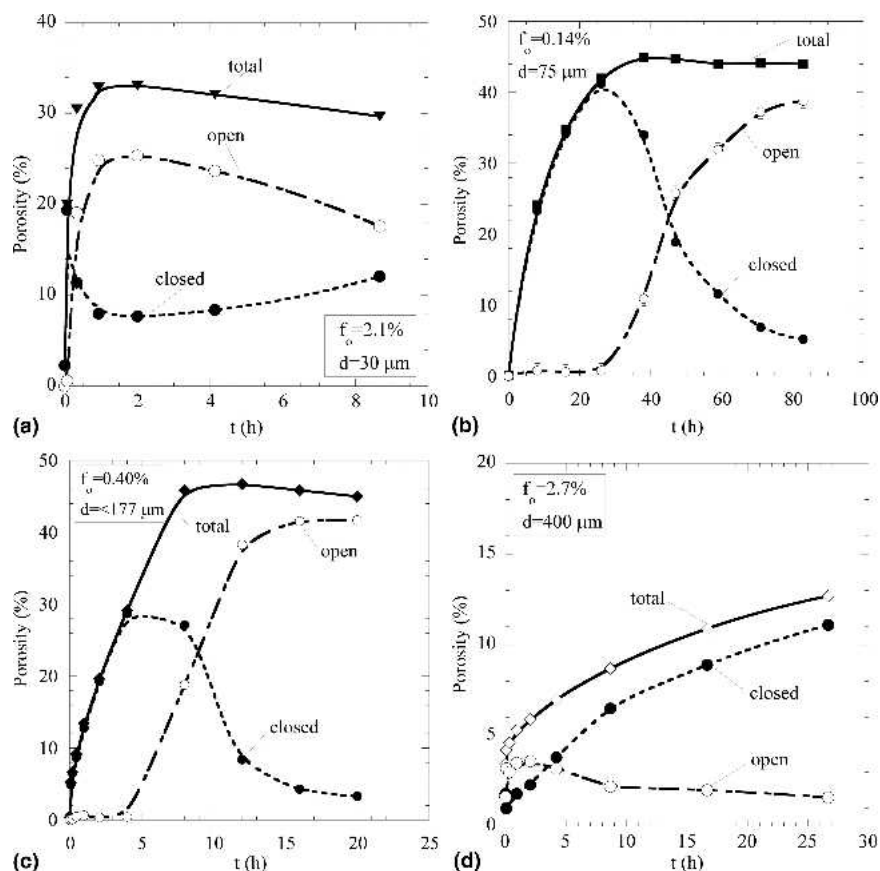
FIG. 5. Total, open, and closed porosity as a function of time during thermal cycling (830–980 °C) for preforms with the following characteristics: (a) fine powders, high porosity ($d = 30$ μm, $f_o = 2.1\%$); (b) intermediate powders, very low porosity ($d = 75$ μm, $f_o = 0.14\%$); (c) unsieved powders, low porosity ($d < 177$ μm, $f_o = 0.40\%$); and (d) coarse powders, high porosity ($d = 400$ μm, $f_o = 2.7\%$).

function of the total porosity in Fig. 6 for all thermally cycled specimens. It is apparent that preforms with very low and low initial porosity ($f_o = 0.06$–0.40%) all maintain closed porosity up to a high value of total porosity (near 45%). Porosity then opens with only small further increase in total porosity, up to ratios F approaching unity. By contrast, preforms with intermediate and high initial porosity ($f_o = 1.3$–2.7%) exhibit porosity opening at total porosity values that are lower (20–35%) for the finest powder preforms ($d = 30$ μm), and much lower (<5%) for the coarsest powder preforms ($d = 400$ μm).

For isothermal foaming (not shown in graph form), almost all of the porosity remains closed throughout foaming for preforms with very low and low initial porosity ($f_o = 0.06$–0.40%): the relative open porosity ratio is $F < 0.14$ after 25 h of isothermal annealing at 903 °C for $f_o = 0.06$ to 0.14% and after 20 h for $f_o = 0.40\%$. Preforms made from the finest powders ($d = 30$ μm) exhibit mostly open porosity after reaching their maximum in total porosity, with $F = 0.90$ for foams with $f_o = 1.3\%$ and $F = 0.75$ for those with $f_o = 2.1\%$. The coarsest powder preforms ($d = 400$ μm) foamed under isothermal conditions exhibit a similar
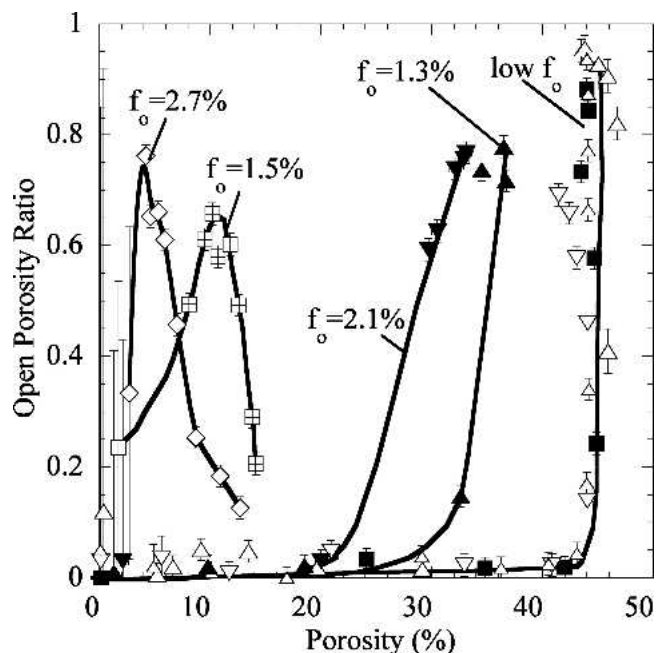

FIG. 6. Relative open porosity ratio as a function of total porosity for all foams made by thermal cycling. The symbols are the same as in Figs. 2 and 3.

open porosity evolution as under thermal cycling conditions [Fig. 5(d)], characterized by a high amount of open porosity during the early stages of foaming followed by a decrease by over a factor two upon further foaming.

B. Foam microstructure

1. Microstructure after thermal cycling

Representative pore structures for thermally-cycled specimens of all four groups of powder sizes and initial preform porosity are shown in Figs. 7(a)–7(d).

For the fine-powder preform with high initial porosity ($d = 30$ μm and $f_o = 2.1\%$), the pores are generally rounded [Fig. 7(a)] and, with a maximum size of about $D = 50$ μm, they are the smallest of all cycled specimens in this study (all pore sizes are listed in Table II). The total porosity is $f_{max} = 35\%$.

A foam made from an intermediate-size powder preform with very low initial porosity ($d = 75$ μm and $f_o = 0.14\%$) is shown in Fig. 7(b) for a total porosity $f_{max} = 42\%$. The porosity is mostly open ($F = 0.88$) and pores have an average size of $D = 300$ μm, with some clusters of interconnected pores in excess of 1000 μm. All pores in the foams made with preforms with intermediate-size powders ($d = 75, 115,$ and 165 μm) and very low initial porosity ($f_o = 0.06$–0.14%) are very jagged.

The pore structure for the unsieved-powder preform with low initial porosity ($d < 177$ μm and $f_o = 0.40\%$) is shown in Fig. 7(c). They are rounded and have a diameter of up to 300 μm. Some coalesced pores are visible, but pores are, in general, more discrete and less jagged than for the very low initial porosity foam [Fig. 7(b)].

A composite micrograph for the coarse-powder preform foams with intermediate initial porosity ($d = 400$ μm and $f_o = 1.5\%$) is shown in Fig. 7(d). The pores appear rounded and smooth, and have the largest size of all samples ($D = 500$ μm). The same preform with higher initial porosity ($f_o = 2.7\%$) results in foams with somewhat smaller average pores size ($D = 300$ μm), but some connected pore clusters are as large as 1000 μm.

2. Microstructure after isothermal foaming

The pore structure for foams produced by isothermal anneal at 903 °C is shown in Figs. 8(a)–8(d), for preforms from all four groups of powder sizes, and three groups of initial preform porosity (very low, low, and high f_o). Figure 8(a) shows a preform with fine powders and high initial porosity ($d = 30$ μm and $f_o = 2.1\%$) after 5.5 h of isothermal foaming: the porosity is $f_{max} = 24\%$ and the average pore size is $D = 20$ μm, but several, much larger pores are also scattered within the matrix. Pores appear less well dispersed than for the corresponding thermally cycled sample [Fig. 7(a)] with higher f_{max}.
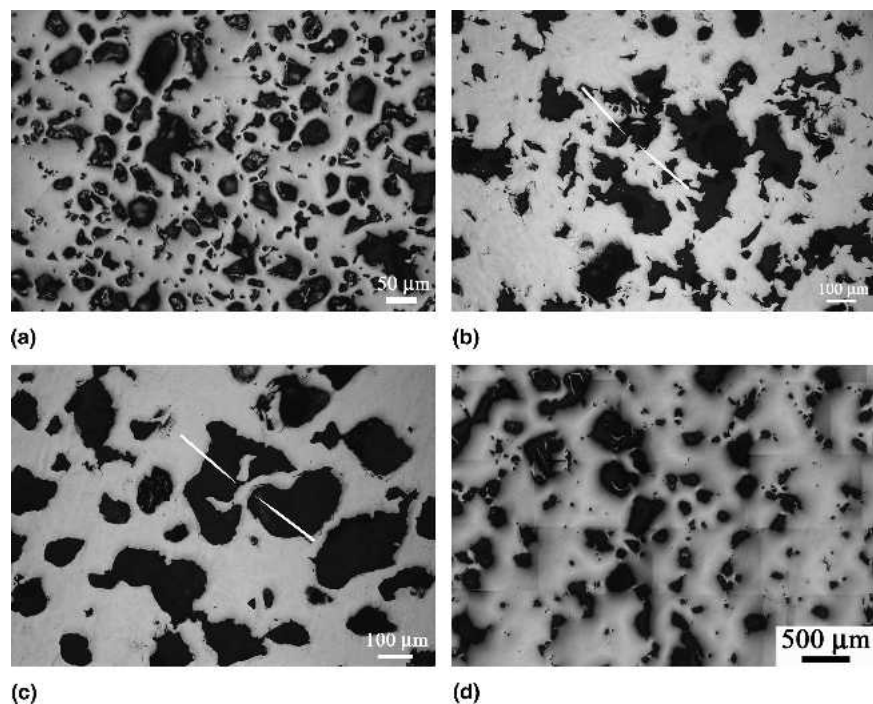

(a) (b) (c) (d)

FIG. 7. Optical micrographs of pore microstructure after thermal cycling foaming (830–980 °C/4 min) for preforms with the following characteristics: (a) fine powders, high porosity ($d = 30$ μm, $f_o = 2.1\%$, $t_{foam} = 9$ h); (b) intermediate powders, very low porosity ($d = 75$ μm, $f_o = 0.14\%$, $t_{foam} = 85$ h); (c) unsieved powders, low porosity ($d < 177$ μm, $f_o = 0.40\%$, $t_{foam} = 20$ h); and (d) coarse powders, intermediate porosity ($d = 400$ μm, $f_o = 1.5\%$, $t_{foam} = 30$ h).
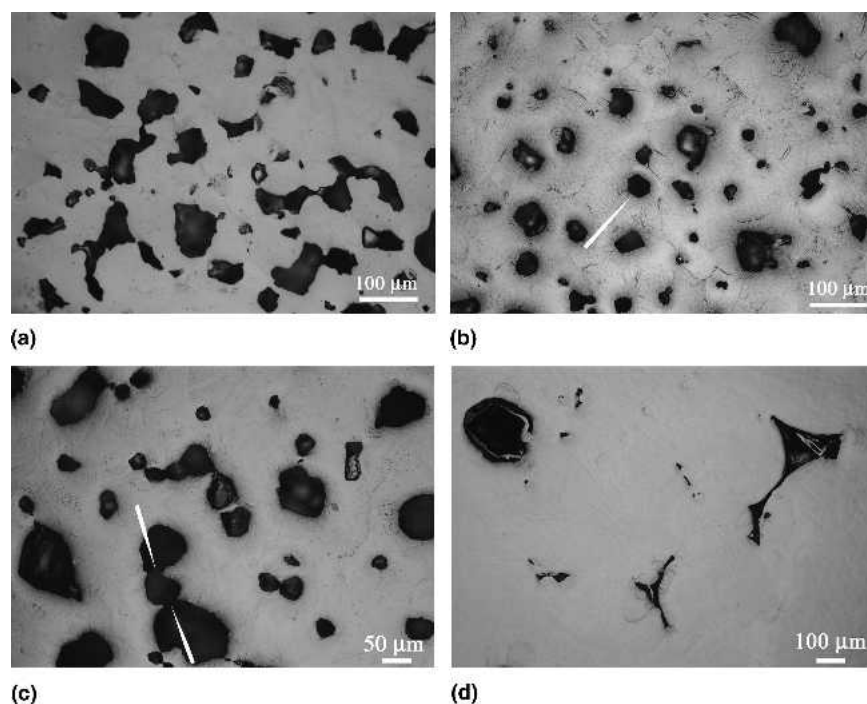
FIG. 8. Optical micrographs of pore microstructure after isothermal foaming (903 °C) for preforms with the following characteristics: (a) fine powders, high porosity ($d = 30$ μm, $f_o = 2.1\%$, $t_{foam} = 5.5$ h); (b) intermediate powders, very low porosity ($d = 75$ μm, $f_o = 0.14\%$, $t_{foam} = 60$ h); (c) unsieved powders, low porosity ($d < 177$ μm, $f_o = 0.40\%$, $t_{foam} = 20$ h); and (d) coarse powders, high porosity ($d = 400$ μm, $f_o = 2.7\%$, $t_{foam} = 13$ h).

Figure 8(b) shows pores after isothermal foaming for 60 h of a preform with intermediate-size powder and very low initial porosity ($d = 75$ μm and $f_o = 0.14\%$). Pores remain discrete and many are faceted, in contrast to the large, ragged pores of the corresponding cycled foam [Fig. 7(b)]. Similar microstructures are observed for the other foams made from intermediate-size powder ($d = 115$ and 165 μm) and very low initial porosity preforms, although the pores become smaller with increasing powder size and decreasing initial porosity.

Figure 8(c) shows the pore structure after 20 h of isothermal foaming for preforms made with unsieved powder and low porosity ($d < 177$ μm and $f_o = 0.40\%$). Several incidences of coalesced pores are observed, as is indicated by arrows in Fig. 8(c), with fewer cases of very thin pore walls observed in the corresponding cycled foam [marked with arrows in Fig. 7(c)].

A foam produced with the coarsest powders and highest initial porosity ($d = 400$ μm and $f_o = 2.7\%$), shown in Fig. 8(d), displays some large, rounded pores and other pores that retain their original as-HIPed shape, and are not expanded, most probably because they were connected to the surface after the powder consolidation step, and were thus unpressurized during the foaming step.

C. Foam stiffness

The Young's and shear moduli, normalized by the Young's modulus of monolithic titanium, are shown in Fig. 9 as a function of total porosity for most of the foams fabricated in the present study by isothermal and cycling foaming. Despite wide variations among samples in pore size, shape, and connectivity (as described in the previous sections), the data points follow a single downward trend. The lowest moduli values are $E{\sim}24$ GPa and $G{\sim}9$ GPa for foams with the highest porosity ($f_{max} = 41$–44%), representing a decrease by a factor 5 compared with monolithic titanium ($E_{Ti} = 120$ GPa and $G_{Ti} = 45$ GPa).

IV. DISCUSSION

A. Foaming kinetics

1. Isothermal foaming

Isothermal foaming curves are characterized by a very rapid initial foaming rate that steadily decreases with time until, in some cases, a terminal porosity is reached (Fig. 2). In an earlier article,[11] we developed an analytical model for foaming that approximates the random array of pressurized pore within the foam matrix by a single spherical pore surrounded by a spherical shell of matrix of the same volume fraction as the foam. There was excellent agreement between this simplified analytical model and a more realistic, finite-element model, considering an infinite three-dimensional pore array within a creeping matrix.[11] The analytical model provides
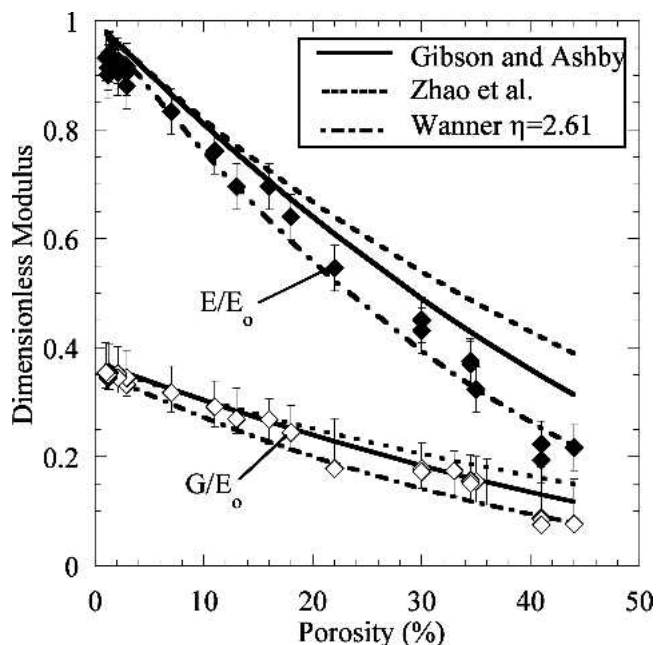
FIG. 9. Young's and shear moduli (normalized with Young's modulus of pore-free titanium) as a function of porosity. Data are compared with model predictions for cellular solids by Gibson and Ashby[20] (solid line) and porous solids by Zhao et al.[21] (dashed line) and Wanner[23] for $\eta = 2.6$.

a differential equation for the foaming rate $\dot{f}(t)$ as a function of the instantaneous pore volume fraction $f(t)$:

$$\dot{f} = \frac{3A}{2} \frac{f(1-f)}{[1-f^{1/n}]^n} \left(\frac{3}{2n} \left| p_e - p_o \frac{f_o}{1-f_o} \frac{1-f}{f} \frac{T_f}{T_o} \right| \right)^n \quad , \tag{1}$$

where f_o is the initial preform pore fraction, p_e is the external pressure (taken here as atmospheric pressure, $p_e = 0.10$ MPa), p_o is the initial pore pressure, T_o is the initial temperature, and T_f is the foaming temperature (here, the ideal gas law is assumed to be operative). In the above equation, A is the power-law creep constant (including the activation energy term) and n is the stress exponent of the solid material, which is assumed to deform under uniaxial conditions according to a power-law, $\dot{\epsilon} = A\sigma^n$, where $\dot{\epsilon}$ is the uniaxial strain rate and σ is the uniaxial applied stress. Assuming that equilibrium densification was reached during the HIP step, the initial gas pressure in the pores can be assumed to be constant and equal to the HIP pressure for all preforms ($p_o = 100$ MPa at $T_o = 1163$ K), independent of the gas pressure (0.33 and 0.70 MPa) used to fill the canisters at ambient temperature. This latter parameter only affects the pore fraction f_o after densification. Thus, in the present study, all parameters in Eq. (1) are constant, except for the initial pore volume fraction f_o.

Using titanium creep parameters from Ref. 17, Eq. (1) was iteratively solved, resulting in foaming curves shown in Fig. 10(a) for initial pore volume fraction f_o

corresponding to the range studied experimentally. The curves exhibit a monotonous reduction in foaming rate with increasing porosity f from the reduction of gas pressure within the expanding pores, which decreases the stress, and thus the deformation rate, of the surrounding matrix. This trend is exhibited in all experimental foaming curves in Fig. 2, which are, in their initial stage when pores are still discrete and spherical, in general agreement with the calculated curves of Fig. 10(a). In particular, Fig. 2 shows that the initial stage of foaming is extremely rapid for foams with intermediate and high porosities. The model also predicts that the initial pore volume fraction f_o strongly affects the foaming curves. This effect is displayed by the experimental foaming curves shown in Fig. 2, where the initial rate of foaming increases with the initial pore fraction, and is very rapid compared with later foaming rates. Finally, the model predicts that the absolute size of the initial pores has no effect on the foaming rate, provided the pore fraction and pressure are constant. This is observed experimentally, too, as the initial portions of the foaming curves in Fig. 2 (before extensive pore merging and opening to the surface) coincide for the preforms with the finest and coarsest powder size with similar initial porosity ($f_o = 1.3$ and 1.5%, respectively), despite initial pore size differing by one order of magnitude ($D_o \sim 7$ and 60 μm, respectively).

Thus, the initial preform porosity f_o is the most important parameter for the initial foaming rate, barring changes in foaming temperature T affecting matrix creep rate or changes in initial pore pressure (affected by the HIP pressure p_o and temperature T_o). The initial preform porosity f_o is itself controlled by the initial gas pressure within the canister and by the packing density of the metal powders in the canister before preform densification. Powder sieving is one important parameter affecting packing density: monosized powders can pack more efficiently than powders with a broad size distribution,[18] thus resulting in a densified preform with low initial porosity. In the present investigation, all but one preforms used sieved powders, albeit with different powder size distribution: the ratio of largest to smallest powder size within a sieved powder batch varied from 1.2 for the intermediate-size 115-μm powders (with a range of 105–125 μm) to 1.5 for the finest 30-μm powders (with a range of 25–37 μm). Additionally, agglomeration and flocculation can occur for fine powders, reducing packing density.[18] Finally, powder shape also strongly affects packing density, which increases with increasingly spherical powders. In the present investigation, all powders were nominally spherical, but much lower packing densities (and thus higher initial preform porosity after densification) could be achieved with less rounded powders, e.g., those produced by the hydride/dehydride technique.
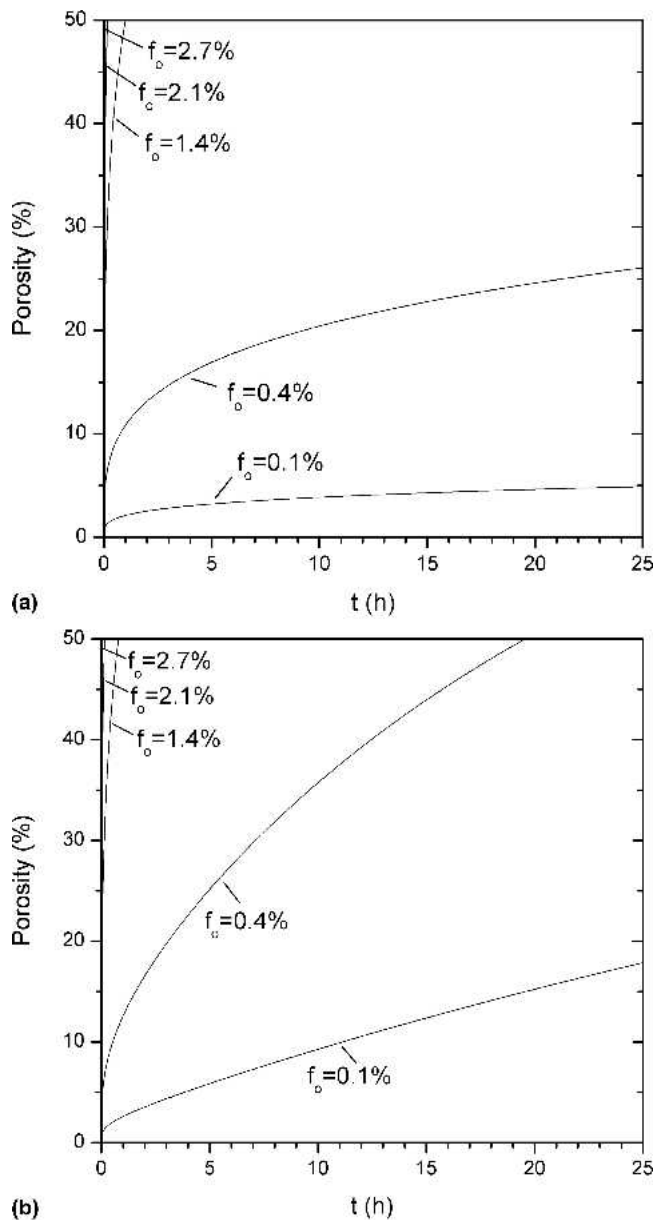
(a)

(b)

FIG. 10. Total porosity as a function of time for (a) isothermal foaming at 903 °C and (b) thermal cycling foaming (830–980 °C). Lines are calculated using Eq. (1) for the initial conditions and initial porosities corresponding to those experimentally studied.

The model also predicts that the final foam porosity increases with increasing initial preform porosity f_o, assuming that foaming ceases because of reduction of the gas pressure from the pore expansion below a point where matrix creep is insignificant. Figure 2 shows that the final porosity (or the porosity after the longest foaming time, for preforms with low and intermediate f_o) increases with increasing initial porosity, except for the preforms made with the coarsest 400-μm powders (with intermediate and high f_o), which achieve unexpectedly low final porosities of 5 to 10%. This departure from the expected

trend can be explained by the significant fraction of open, unpressurized pores present after consolidation in these preforms. They further lost most of their remaining entrapped argon by pore opening early in the foaming process, in a manner similar to that shown in Fig. 6 for thermal cycling foaming. This may be from the stress concentrations from the angular shape of the initial pores present between previous metal particles [Fig. 1(d)]. In contrast to the coarsest 400-μm powder preforms, the preforms made with the finest 30-μm powders show much higher final porosity, despite having the same range of initial porosity. This correlates with the fully closed initial porosity and rounder pore shape exhibited in the preforms before foaming, both resulting from the reduced diffusion flux needed to spheroidize the much smaller pores during HIP consolidation. These results indicate that improving the resistance against premature pore merging by producing more rounded initial pores (e.g., by using higher HIP densification time or temperature, or smaller particle size) should lead to higher final porosity for preforms with intermediate and high initial porosity.

2. Thermal-cycling foaming

Equation (1) can be modified to take into account the contribution of transformation superplasticity to foaming.[11] Solving this equation iteratively for various initial porosities results in the curves of Fig. 10(b), which can be compared with the experimental thermal-cycling foaming curves of Fig. 3; the agreement is semiquantitative, as expected from the severe simplifications used in the model (e.g., regular array of monosized spherical pores which grow without merging). As for isothermal foaming, the trend of initial foaming rate and final porosity increasing with the initial preform porosity is present during thermal cycling in Fig. 3, except for preforms that prematurely loose their entrapped gas from pore opening to the surface, i.e., preforms with intermediate and high initial porosity ($f_o = 1.3$–2.7%).

The best overall foaming characteristics, as defined by the highest final porosity (47%) reached in the shortest time (12 h), are achieved by the preform with low porosity ($f_o = 0.40$%) made with unsieved powders. This preform strikes a good balance between high initial foaming rate [which increases rapidly with f_o, Fig. 10(b)] and low tendency for pores to open prematurely to the surface, which limits the final porosity (and occurs at high f_o). The second best performance is achieved by a preform with intermediate initial porosity ($f_o = 1.3$%, made with the finest 30-μm powders), which reaches over 36% porosity is as little as 2 h of foaming. It is likely that a preform with initial porosity between these two values ($f_o = 0.40$ and 1.3%) and with rounded, closed initial porosity will display an even better combination of average foaming rate and final porosity.

Assuming that no gas escapes during foaming, the final porosity f_f can be found by volume conservation as[7]

$$f_f = \frac{s}{s + f_o^{-1} - 1} \quad , \qquad (2)$$

where $s = p_o T_f / p_f T_o$ is the ratio of the pore volumes (using the ideal gas law) after foaming and before foaming (i.e., after HIP densification). For the present initial conditions (HIP pressure $p_o = 100$ MPa, HIP temperature $T_o = 1163$ K, and foaming temperature $T_f = 1176$ K), an upper bound for the final porosity is found from Eq. (2), assuming that the pore pressure is the same as the external pressure ($p_f = 0.1$ MPa); in practice, foaming will become immeasurably slow for pore pressures that are higher than this value. This maximum attainable porosity predicted by Eq. (2) is $f_f = 38$ to 58% for the preforms with lowest initial porosity ($f_o = 0.06$–0.14%), close to the observed values (Table II). This suggests that little argon escapes by pore coalescence before the pores are nearly fully expanded, as confirmed by Fig. 5(b), showing that total porosity has reached a plateau near the time when porosity starts to open. By contrast, Eq. (2) predicts final porosities $f_f = 80\%$ and 93 to 97% for preform with low initial porosity ($f_o = 0.40\%$) and intermediate or high initial porosity ($f_o = 1.3$–2.7%), respectively. Indeed, Figs. 5(a), 5(c), and 5(d) show that open porosity appears well before the foaming curves reached a plateau, indicating that much higher porosities could be achieved if pore coalescence was inhibited.

The increase in pore opening without concomitant increase in total porosity displayed by foams with very low and low initial porosities [Figs. 5(b) and 5(c)] is related to the low gas pressure present in the pores after the foaming curve achieves a plateau: the matrix stresses are too low to create significant changes in overall porosity, but are sufficient to produce localized deformation and eventual fracture of the very thin pore walls present at high porosity levels [arrows in Fig. 7(b)]. Thus, thermal cycling beyond the time at which total porosity reaches a plateau can be used to increase the pore connectivity in these foams. A foam with closed-pore architecture is stronger and stiffer, and thus more desirable for structural applications, whereas open-pore foams are desirable in applications such as filters, catalyst substrates, or biomedical implants.

3. Deformation mechanism

Figures 10(a) and 10(b) show that significantly higher foaming rates are predicted under cycling superplastic conditions compared with isothermal creep conditions at the effective temperature. Comparison of experimental foaming curves (Figs. 2 and 3) clearly demonstrates that superplastic conditions lead, in all cases, to faster foaming and higher final porosity. The comparison is facilitated in Figs. 4(a)–4(d) where thermally cycled curves can be directly compared with isothermal curves at the effective temperature (903 °C); if thermal cycling did not activate superplastic deformation, the two curves would coincide.

The foaming improvement achieved during thermal cycling has been previously demonstrated and discussed for CP-Ti and Ti-6Al-4V foams[7–12] and reflects the two advantages of superplastic deformation compared with creep deformation. First, under superplastic conditions, higher matrix deformation rates are achieved at a given stress, resulting in higher foaming rates at a given pore pressure. Second, superplastic deformation allows for higher fracture strain as a result of reduced necking and cavitation. Thus, foaming under superplastic conditions, which inhibits the fracture of walls separating neighboring pores, leads to pore coalescence to the surface and gas escape, which explains the higher final porosity compared with nonsuperplastic conditions.

However, the superplastic foaming enhancement varies among the various preforms studied. Preforms with high and intermediate initial porosity [Figs. 4(a) and 4(d)] show a smaller enhancement than preforms with low or very low initial porosity [Figs. 4(b) and 4(c)]. During the early stages of foaming, the pore pressures are very high, leading to a high volume fraction of matrix subjected to stresses large enough for power-law creep to dominate over transformation superplasticity. Preforms then foam at the same rate (and their pore walls fracture at the same rate), whether they are being thermally cycled or isothermally held at the effective temperature, as also visible in the calculated curves of Figs. 10(a) and 10(b). As pores expand, the fraction of matrix deforming by power-law creep decreases while that deforming by superplasticity increases, until superplasticity becomes the overall dominant deformation mechanism, and the associated advantages (faster rate and higher strain) become operative. This transition from initial creep-controlled foaming to subsequent superplastic-control foaming occurs earlier for the low initial porosity preforms, for which the benefits of superplastic foaming can then accrue longer, leading to clearer differences between the isothermal and cyclic foaming curves. Finally, another reason for the low superplastic enhancement in Fig. 4(a) is that the cycling period (20 min) was five times longer than those used in Figs. 4(b)–4(d), thus reducing by the same factor the superplastic contribution to foaming.

B. Foam microstructure

Micrographs of selected foamed specimens, shown in Fig. 7 for thermal cycling and Fig. 8 for isothermal foaming, illustrate that pores are larger for the superplastic foaming condition, as expected from the higher pore volume fraction.

The pores resulting from the lowest initial porosity preforms are very large and jagged after thermal cycling [Fig. 7(b)] compared with the facetted pores of the corresponding isothermal foam [Fig. 8(b)]. This is evidence of the continued microscale deformation during superplastic foaming, allowing for fracture of the pore walls and opening of porosity, even as total porosity remains constant [Fig. 5(b)]. As the initial porosity decreases from f_o = 0.14% to f_o = 0.06%, the pore size and jaggedness increase, as expected from the larger distance between pores. Conversely, upon increasing initial porosity to f_o = 0.40, the pores in the superplastic foams [Fig. 7(c)] are much more rounded compared with those in Fig. 7(b). Here, the absolute initial pore size may explain this effect: for the same final pore size of 300 μm, the foam in Fig. 7(b) with smaller initial pores (D_o = 6 μm) must have exhibited more extensive pore coalescence than that in Fig. 7(c) with initial pores larger by a factor 2 (D_o = 12 μm).

Despite having different initial high porosities (f_o = 1.3 and 2.1%), the two finest powders (d = 30 μm) preforms result, after thermal cycling, in foams with very similar final porosities (35 and 30%) and pore morphology [rounded shape, about 50 μm in size, and good spatial distribution, as illustrated in Fig. 7(a)]. The final pore size is smaller for these foams than any other foam in this study, except for the isothermally foamed corresponding specimens, which has 25-μm pores [Fig. 8(a)]. This is expected from the high number density of initial pore and the relatively low level of pore coalescence. The small pore size also explains the downward trend of total and open porosities [Fig. 5(a)] upon cycling beyond 2 h: once the gas has escaped from the pores, they are free to sinter, which occurs faster with smaller pores, thus making densification visible in the foaming curve of Fig. 5(a).

Conversely, high initial porosity foams made from the coarsest powder preform (d = 400 μm) have the largest pores, under isothermal and thermal cycling conditions [Figs. 7(d) and 8(d)], despite having the lowest final porosity. This is because of their initial pore size, which is much larger than all other preforms (Table II). Here, too, the open porosity decreases after reaching a maximum value after about 2 h [Fig. 5(d)], but without an simultaneous decrease in total porosity. A possible explanation for this behavior is that depressurized pore clusters loose their connection to the surface when small necks between pores are closed by sintering or by matrix flow from the expansion of neighboring pores.

C. Foam elastic properties

As shown in Fig. 9 for foams produced under isothermal creep conditions and cycling superplastic conditions, the foam Young's modulus E and shear modulus G decrease monotonically with increasing porosity. Gibson

and Ashby[20] derived the following expressions for the moduli of foams

$$\frac{E}{E_o} = \left(\frac{\rho}{\rho_o}\right)^2 \quad , \tag{3a}$$

$$\frac{G}{G_o} = \left(\frac{\rho}{\rho_o}\right)^2 \quad , \tag{3b}$$

where ρ is the density and the subscript o demotes the monolithic material. These equations are derived for cellular materials with struts deforming in bending, but have been found to predict metallic foam stiffness over a broad range of porosity, albeit with considerable amounts of scatter.[20] A more rigorous approach by Zhao et al.,[21] based on the Mori-Tanaka theory for composites, provides an upper bound prediction[22] for the foam bulk modulus K and shear modulus G by considering isolated, spherical voids with zero stiffness within an elastic matrix

$$\frac{K}{K_o} = 1 - \frac{f}{1 - (1 - f)\alpha_o} \quad , \tag{4a}$$

$$\frac{G}{G_o} = 1 - \frac{f}{1 - (1 - f)\beta_o} \quad , \tag{4b}$$

where $f = 1 - \rho/\rho_0$ is the volume fraction of pores and the two coefficients α_o and β_o are given as $\alpha_o = (1 + \upsilon)/3(1 - \upsilon)$ and $\beta_o = 2(4 - 5\upsilon)/15(1 - \upsilon)$, with υ as the matrix Poisson's ratio. For isotropic foams, the Young's modulus can then be calculated from Eqs. 4(a) and 4(b) as

$$E = \frac{9\mu K}{\mu + 3K} \quad . \tag{5}$$

As shown in Fig. 9, both models nearly coincide and provide a good description of the measured foam stiffness when porosity is below 18%, for which pores can be assumed to be near spherical and isolated. At higher porosities, the measured moduli are below the predictions, probably as a result of elongated pore clusters from pore merging. For nonspherical pores, Wanner[23] proposed to replace the exponent 2 in Eqs. 3(a) and 3(b) with an exponent $\eta > 2$, tending toward infinity for sharp cracks aligned perpendicular to the loading axis. A best fit with our data is obtained using η = 2.6, as shown in Fig. 9. This is close to the original exponent η = 2, confirming our current and previous[7–11] metallographic observations that pores are not strongly elongated or aligned.

Another possible reason for the deviation of the data from the predictions at high porosity is the jagged shape of the pores [Fig. 7(b)]. Remains of fractured pore walls that jut into the pores clusters supports less (or no) mechanical load, so the effective foam porosity, which considers only the load-bearing portion of the matrix, is higher than that measured from density. This adjustment

in porosity would translate the data points to higher porosities in Fig. 9, improving agreement with Eqs. 3(a) and 3(b) and 4(a) and 4(b).

The Young's moduli measured for higher porosity foams ($E = 20$–22 GPa for porosities of 41–44%) are close to the stiffness of higher density cortical bone (~19 GPa) and are only about twice that of trabecular bone (~10 GPa).[24,25] Better matching of elastic moduli should decrease stress-shielding in bone-replacement implants, thus reducing the amount of implant loosening and increasing the life of the implant.[26,27] Also, open porosity may allow for bone ingrowth, thus further improving implant fixation. However, before porous titanium such as those described here can be considered for implants, other properties must also be considered, e.g., wear and corrosion resistance, static and fatigue strength, as well as ductility and toughness.

V. CONCLUSIONS

Solid-state foaming of unalloyed titanium, based on expansion of pressurized pores, was characterized under isothermal and thermal cycling conditions, where the matrix deformation mechanisms are creep with and without additional transformation superplasticity, respectively. The initial size and fraction of the pressurized pores in the preforms were varied by using metal powders with various size and distributions, and two levels of argon backfill pressure. The following conclusions can be drawn.

(1) For isothermal foaming, foaming rates increase with increasing initial porosity, in agreement with a simple analytical model. However, final porosity is limited by the low creep rates of the matrix at 903 and 980 °C for preforms with low initial porosity, and by premature pore merging to the specimen surface for preforms with high initial porosity. Pore merging is further accentuated in preforms with large initial pore size.

(2) Thermal cycling (830–980 °C), which activates transformation superplasticity as an additional deformation mechanism, results in higher foaming rates and final porosity compared with isothermal foaming at the corresponding effective temperature (903 °C), in agreement with model predictions. These improvements are because of the lower flow stress and higher ductility achievable under superplastic conditions, and are most marked for preforms with low initial porosity, for which superplasticity dominates over creep deformation during foaming.

(3) The foam Young and shear moduli decrease quadratically with relative density up to porosities of 18%, in agreement with existing models, and more rapidly up to porosities of 44% because of the nonspherical shape of the pores. Values of the Young's modulus as low as 20 GPa are measured for foams with 44% open porosity, making these foams interesting for bone implants.

REFERENCES

1. D.C. Dunand: Processing of titanium foams. *Adv. Eng. Mater.* **6,** 369 (2004).
2. M.W. Kearns, P.A. Blenkinsop, A.C. Barber, and T.W. Farthing: Manufacture of a novel porous metal. *Int. J. Powder Metall.* **24,** 59 (1988).
3. D.T. Queheillalt, B.W. Choi, D.S. Schwartz, and H.N.G. Wadley: Creep expansion of porous Ti-6Al-4V sandwich structures. *Metall. Mater. Trans. A* **31,** 261 (2000).
4. D.T. Queheillalt, K.A. Gable, and H.N.G. Wadley: Temperature dependent creep expansion of Ti-6Al-4V low density core sandwich structures. *Scripta Mater.* **44,** 409 (2001).
5. D.M. Elzey and H.N.G. Wadley: The limits of solid state foaming. *Acta Mater.* **49,** 849 (2001).
6. R. Vancheeswaran, D.T. Queheillalt, D.M. Elzey, and H.N.G. Wadley: Simulation of the creep expansion of porous sandwich structures. *Metall. Mater. Trans. A* **32,** 1813 (2001).
7. N.G. Davis, J. Teisen, C. Schuh, and D.C. Dunand: Solid-state foaming of titanium by superplastic expansion of argon-filled pores. *J. Mater. Res.* **16,** 1508 (2001).
8. N.G.D. Murray and D.C. Dunand: Microstructure evolution during solid-state foaming of titanium. *Compos. Sci. Technol.* **63,** 2311 (2003).
9. N.G.D. Murray, C.A. Schuh, and D.C. Dunand: Solid-state foaming of titanium by hydrogen-induced internal-stress plasticity. *Scripta Mater.* **49,** 879 (2003).
10. N.G.D. Murray and D.C. Dunand: Effect of thermal history on the superplastic expansion of argon-filled pores in titanium: Part 1—Kinetics and microstructure. *Acta Mater.* **52,** 2269 (2004).
11. N.G.D. Murray and D.C. Dunand: Effect of thermal history on the superplastic expansion of argon-filled pores in titanium: Part 2—Modeling of kinetics. *Acta Mater.* **52,** 2279 (2004).
12. H.L. Li, S.M. Oppenheimer, S.I. Stupp, D.C. Dunand, and L.C. Brinson: Effects of pore morphology and bone ingrowth on mechanical properties of microporous titanium as an orthopaedic implant material. *Mater. Trans.* **45,** 1124 (2004).
13. M.F. Ashby, A. Evans, N.A. Fleck, L.J. Gibson, J.W. Hutchinson, and H.N.G. Wadley: *Metal Foams: A Design Guide* (Butterworth-Heinemann, Boston, 2000).
14. G.W. Greenwood and R.H. Johnson: The deformation of metals under stress during phase transformations. *Proc. R. Soc. London* **283A,** 403 (1965).
15. P. Zwigl and D.C. Dunand: Transformation superplasticity of zirconium. *Metall. Mater. Trans. A* **29,** 2571 (1998).

16. D.C. Dunand and C.M. Bedell: Transformation-mismatch super-plasticity in reinforced and unreinforced titanium. *Acta Mater.* **44,** 1063 (1996).

17. H.J. Frost and M.F. Ashby: *Deformation-Mechanism Maps: The Plasticity and Creep of Metals and Ceramics* (Pergamon Press, Oxford, 1982).

18. J.S. Reed: *Introduction to the Principles of Ceramic Processing* (John Wiley, New York, 1988).

19. J.D. Eshelby: The determination of the elastic field of an ellipsoidal inclusion, and related problems. *Proc. R. Soc. London* **A241,** 376 (1957).

20. L.J. Gibson and M.F. Ashby: *Cellular Solids* (Cambridge University Press, 1997).

21. Y.H. Zhao, G.P. Tandon, and G.J. Weng: Elastic-moduli for a class of porous materials. *Acta Mech.* **76,** 105 (1989).

22. G.J. Weng: The theoretical connection between Mori Tanaka theory and the Hashin Shtrikman Walpole bounds. *Int. J. Engng. Sci.* **28,** 1111 (1990).

23. A. Wanner: Elastic-modulus measurements of extremely porous ceramic materials by ultrasonic phase spectroscopy. *Mater. Sci. Eng. A* **248,** 35 (1998).

24. J.Y. Rho, R.B. Ashman, and C.H. Turner: Young's modulus of trabecular and cortical bone material—ultrasonic and microtensile measurements. *J. Biomech.* **26,** 111 (1993).

25. R.B. Ashman and J.Y. Rho: Elastic-modulus of trabecular bone material. *J. Biomech.* **21,** 177 (1988).

26. M.J. Donachie: Biomedical alloys. *Adv. Mater. Proc.* **7,** 63 (1998).

27. S.J. Simske, R.A. Ayers, and T.A. Bateman: Porous materials for bone engineering. *Mater. Sci. Forum* **250,** 151 (1997).